Supplementary Information for

The quantity of ligand-receptor interactions between nanoparticles and target cells

Kathrin Schorr[1], Sebastian Beck[1], Oliver Zimmer[1], Felix Baumann[1], Max Keller[2], Ralph Witzgall[3], Achim Goepferich[1]

[1]Department of Pharmaceutical Technology, University of Regensburg, 93053 Regensburg, Bavaria, Germany. (K. Schorr: kathrin.schorr@ur.de), (S. Beck: sebastianbeck@magenta.de), (O. Zimmer: oliver.zimmer@ur.de), (F. Baumann: felix.baumann@ur.de)
[2]Department of Pharmaceutical Chemistry, University of Regensburg, 93053 Regensburg, Bavaria, Germany. (M. Keller: max.keller@ur.de)
[3]Institute for Molecular and Cellular Anatomy, University of Regensburg, 93053 Regensburg, Bavaria, Germany. (R. Witzgall: ralph.witzgall@vkl.uni-regensburg.de)

*Achim Goepferich
Email: achim.goepferich@ur.de
Phone: +49 941 943-4842

Author Contributions: A.G., M.K., R.W., K.S., S.B. and O.Z. designed research; M.K., K.S., F.B. and O.Z. performed research; K.S. analyzed data; A.G. and K.S. wrote the paper; A.G. supervised the project.

Keywords: engineered nanoparticles, number of binding ligands, nanoparticle-cell interaction, viral role models, receptor clustering, nanoparticle binding in clathrin coated pits

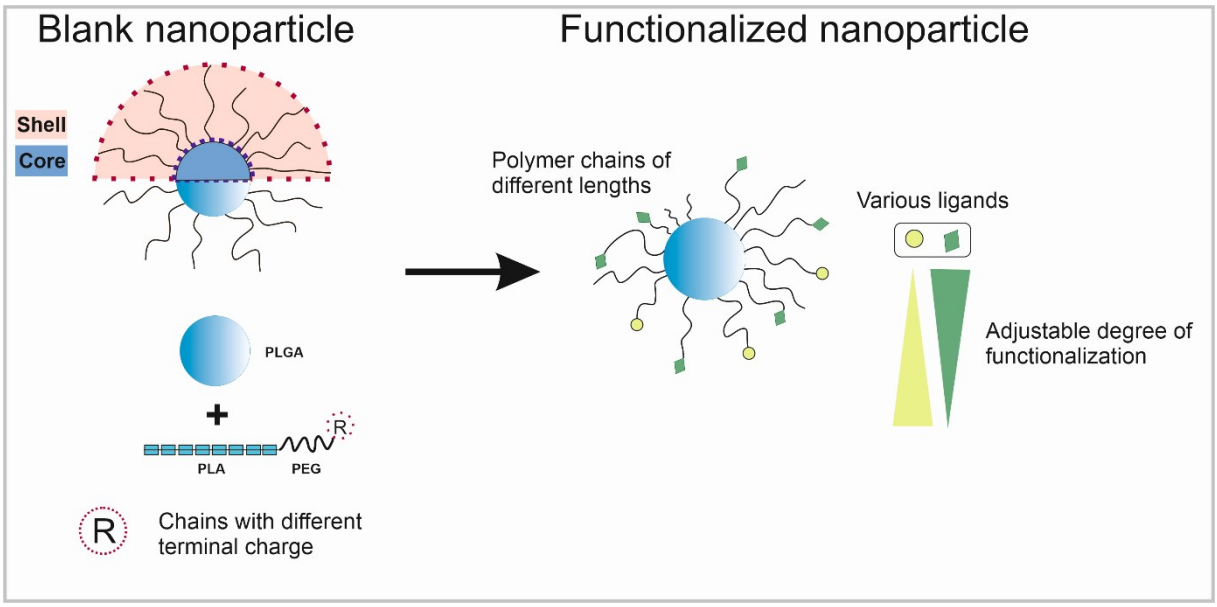

Figure S 1 Illustration of the nanoparticle design concept and its high degree of modularity in both polymer chain construction and functionalization. The polymeric nanoparticles, well established in our group [1–4] and used as model system for the present work, are composed as core-shell nanoparticles with biocompatible and biodegradable polymers selected for both, the shell, and the core. The use of PLGA in the core enables the incorporation of fluorescent dyes into the nanoparticles. PLA-PEG block copolymer chains can be synthesized with different molecular weights and functionalized with a variety of small molecule or peptidic ligands, whereby the degree of functionalization can be adapted to the target. By selecting multiple ligands that address common target cells, hetero-multivalent systems can be created. To achieve the highest possible target cell specificity and selectivity, the nanoparticle designs are inspired by viral role models, as viruses are known to be the most efficient particulate systems in nature. The modularity on which the general nanoparticle design concept is based makes the implementation of such complex targeting strategies feasible and the nanoparticles a promising platform technology which is worth to be further investigated.

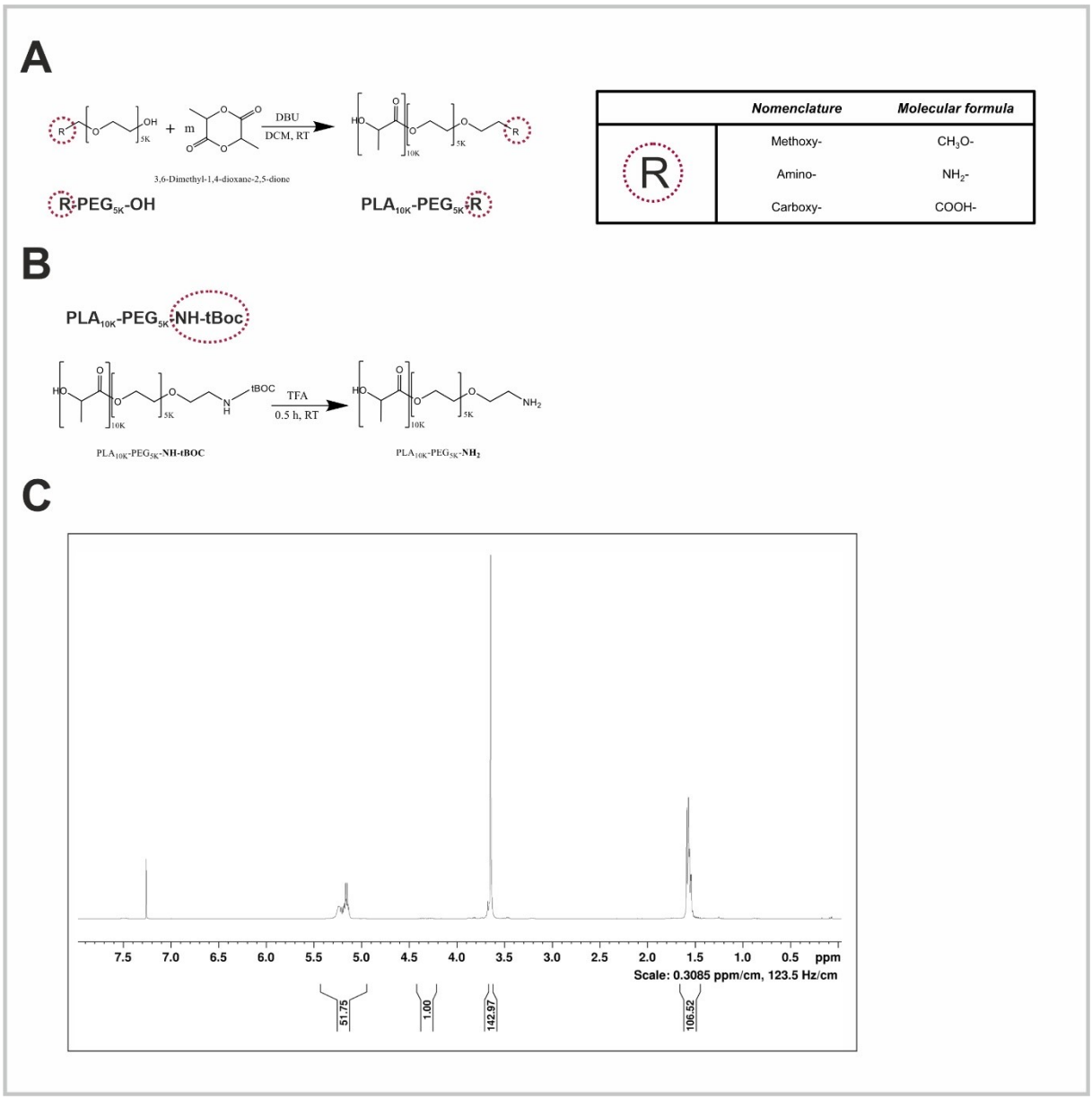

Figure S 2 Block copolymer synthesis, modification, and characterization. (A) Reaction equation for the synthesis of PEG-PLA block copolymers through ring opening polymerization of the cyclic lactone 3,6-dimethyl-1,4-dioxane-2,5-dione with polyethylene glycol chains as macroinitiators for the reaction. The block copolymers can be synthesized with different terminal charges referred as head groups *(R)*. (B) Reaction equation for the deprotection of *tert*-butyloxycarbonyl (*t*Boc)-protected block copolymer. (C) Exemplary *^{1}H*-NMR spectrum (400 MHz, $CDCl_3$) of NH_2-PEG_{5K}-PLA_{10K} block copolymer.

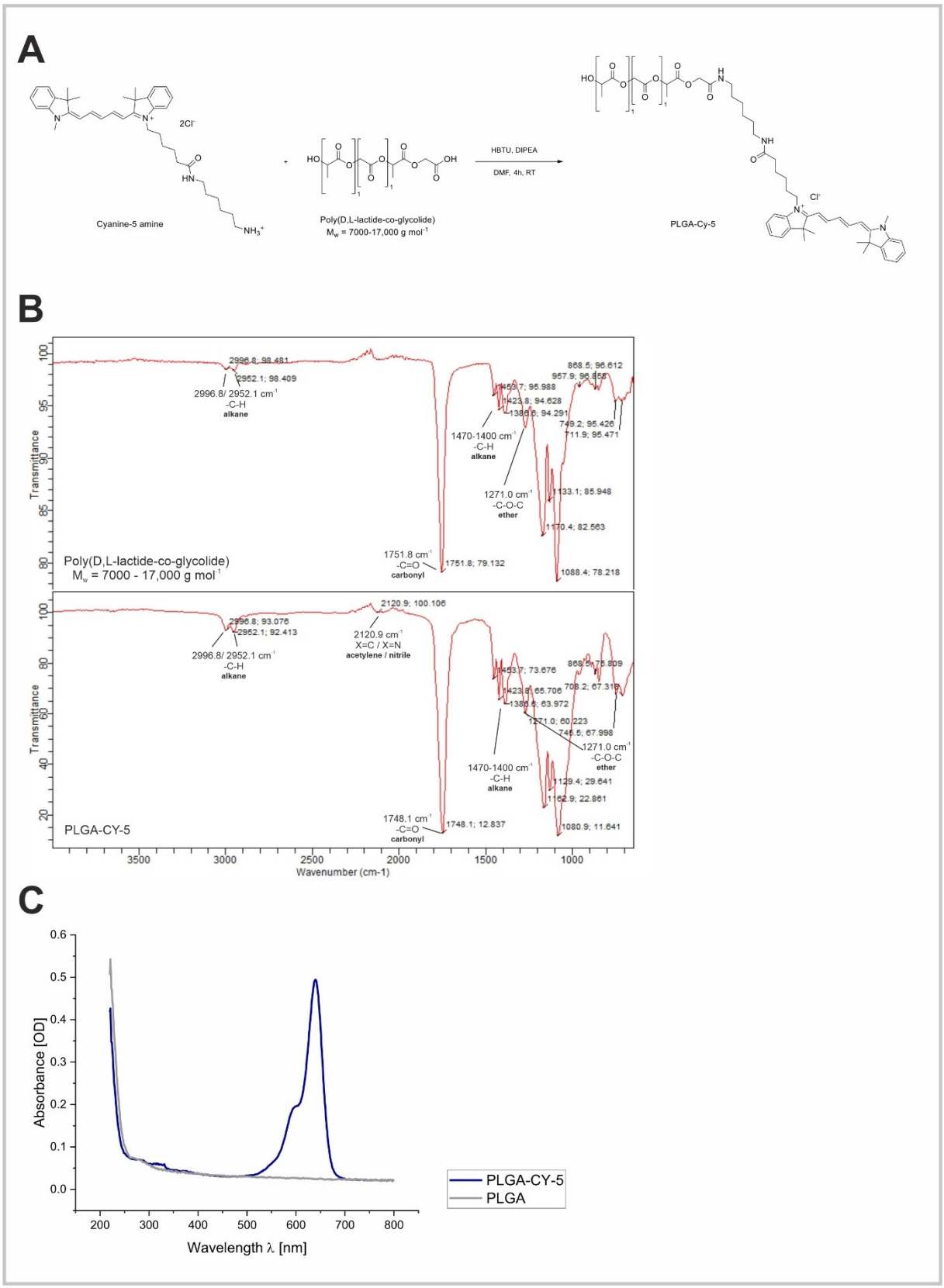

Figure S 3 Fluorescence labeling of PLGA with CY-5. (A) Reaction equation of fluorescence labeling of PLGA with CY-5. (B) FTIR spectra of PLGA (M_w = 7000-17,000 g mol^{-1}) and PLGA-CY-5. A peak for acetylene/ nitrile (2128.3 [cm^{-1}] ν (X=C/ X=N)) was found in the spectrum of PLGA-CY-5. (C) Absorbance spectra of PLGA und PLGA-CY-5 (4 mg mL^{-1} in acetonitrile). The spectrum of PLGA-CY-5 exhibits a characteristic peak of CY-5 at a wavelength of λ 640 nm.

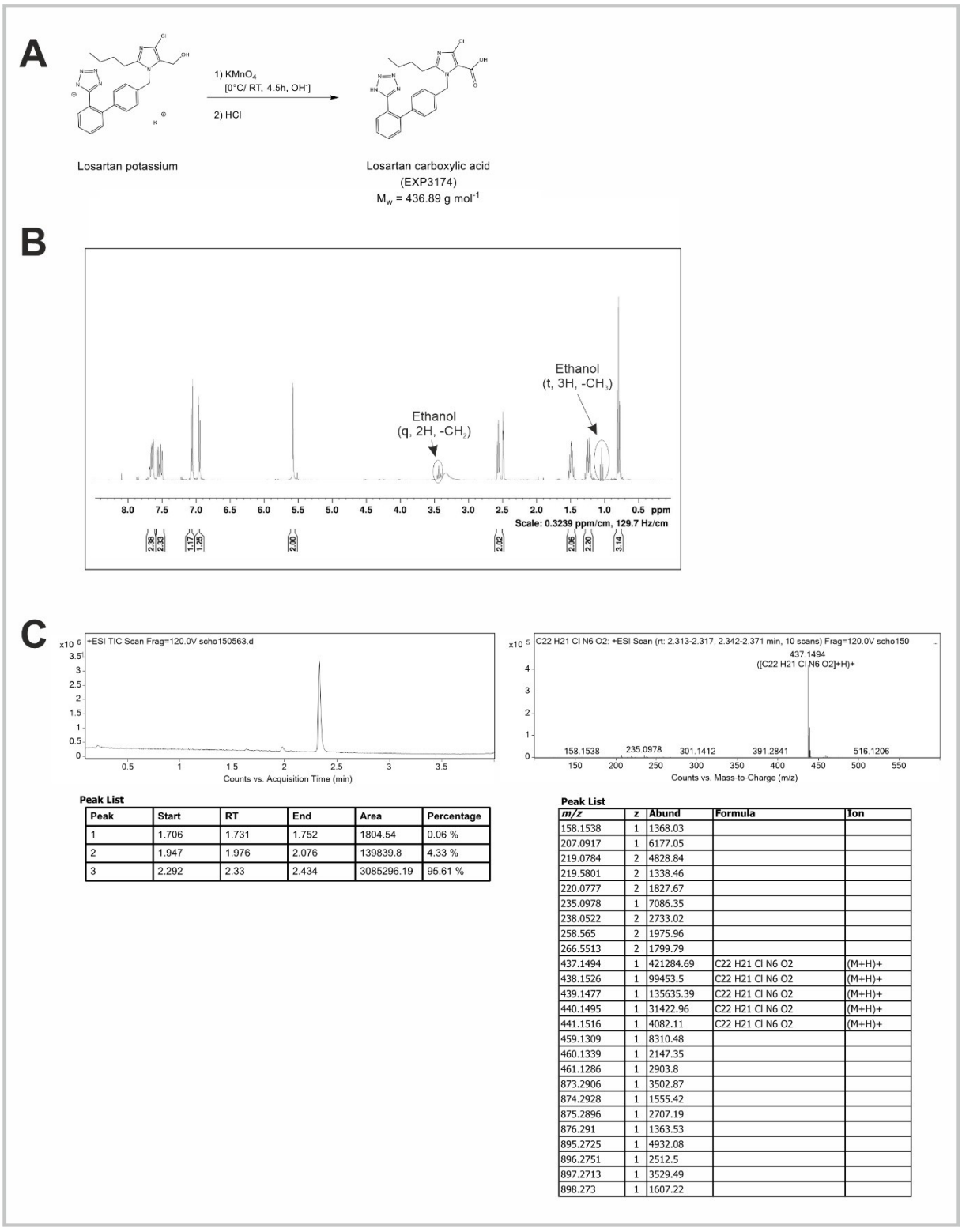

Peak List

Peak	Start	RT	End	Area	Percentage
1	1.706	1.731	1.752	1804.54	0.06 %
2	1.947	1.976	2.076	139839.8	4.33 %
3	2.292	2.33	2.434	3085296.19	95.61 %

Peak List

m/z	z	Abund	Formula	Ion
158.1538	1	1368.03		
207.0917	1	6177.05		
219.0784	2	4828.84		
219.5801	2	1338.46		
220.0777	2	1827.67		
235.0978	1	7086.35		
238.0522	2	2733.02		
258.565	2	1975.96		
266.5513	2	1799.79		
437.1494	1	421284.69	C22 H21 Cl N6 O2	(M+H)+
438.1526	1	99453.5	C22 H21 Cl N6 O2	(M+H)+
439.1477	1	135635.39	C22 H21 Cl N6 O2	(M+H)+
440.1495	1	31422.96	C22 H21 Cl N6 O2	(M+H)+
441.1516	1	4082.11	C22 H21 Cl N6 O2	(M+H)+
459.1309	1	8310.48		
460.1339	1	2147.35		
461.1286	1	2903.8		
873.2906	1	3502.87		
874.2928	1	1555.42		
875.2896	1	2707.19		
876.291	1	1363.53		
895.2725	1	4932.08		
896.2751	1	2512.5		
897.2713	1	3529.49		
898.273	1	1607.22		

Figure S 4 Synthesis and confirmation of identity and purity of losartan carboxylic acid (EXP3174). (A) Reaction equation for the synthesis of EXP3174 obtained by oxidation of losartan with potassium permanganate. (B) *1H*-NMR spectrum (400 MHz, DMSO-d_6) of EXP3174. (C) LC-MS chromatogram showed purity of the product of > 95 %. The mass of 437.1494 (MH^+) corresponding to EXP3174 was found.

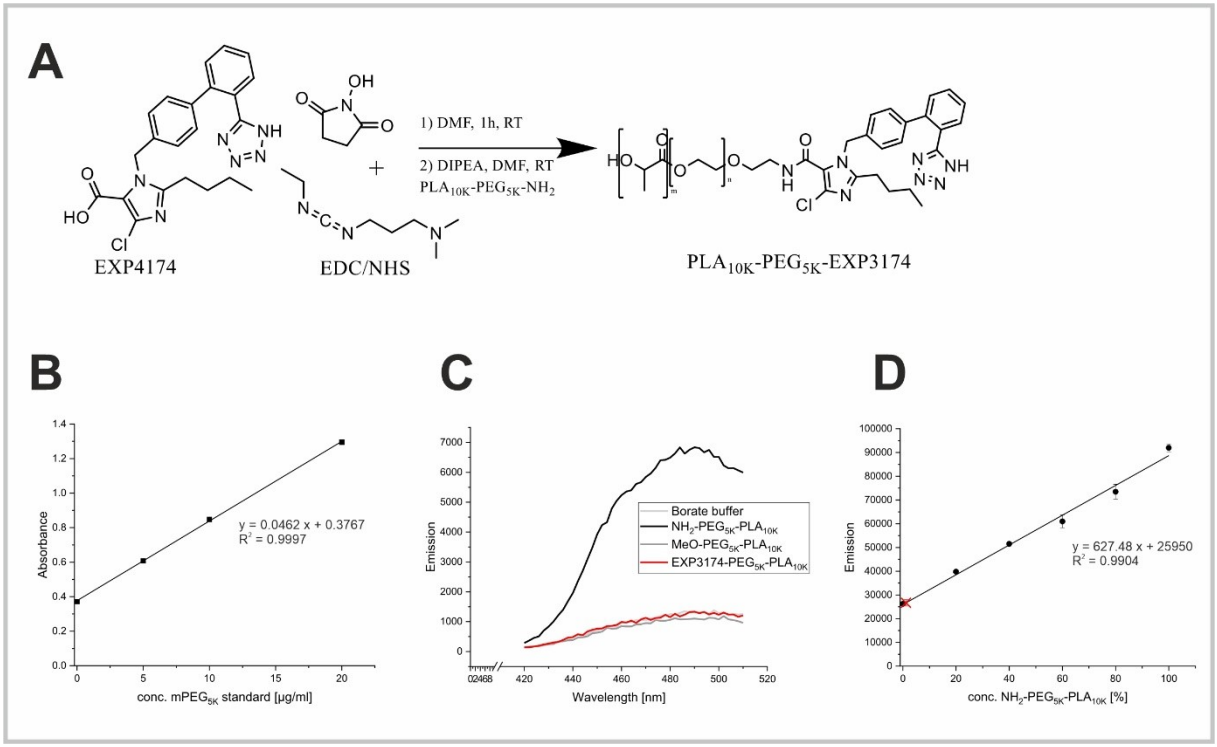

Figure S 5 Demonstration of the coupling efficiency of EXP3174 to the NH_2-PEG_{5K}-PLA_{10K} block copolymer. (A) Reaction equation for the coupling of EXP3174 to the polymer via EDC/NHS chemistry. (B) Preparation of polymer micelles of NH_2-PEG_{5K}-PLA_{10K}, MeO-PEG_{5K}-PLA_{10K} and EXP3174-PEG_{5K}-PLA_{10K} by emulsification-solvent evaporation method for determining the degree of EXP3174-functionalization on the polymer. Plotting a calibration curve against a $mPEG_{5K}$ standard to normalize the micelle concentrations according to their PEG content determined by *Iodine assay*. (C) Detection of free amino groups in the samples through *Fluram assay*. Recording of emission spectra after addition of borate buffer and fluorescamine to the samples (fixed excitation: λ = 380/10 nm; emission start: λ = 420/10 nm; emission stop: λ = 510 nm; step: 2 nm; recorded on a Synergy Neo 2 Multi-Mode Microplate Reader). In addition, the sample background was captured by recording an emission spectrum of borate buffer after addition of fluorescamine under the same measurement conditions. The measured emission of the EXP3174-functionalized polymer was in the order of magnitude of the background and the amino group free MeO-PEG_{5K}-PLA_{10K} micelles. (D) Plotting a calibration line for the degree of free amino groups by measuring the fluorescence of methoxy- and amino-terminated polymer micelles at specific concentration ratios (amino- to methoxy-terminated, 100:0 / 80:20 / 60:40 / 40:60 / 20:80 / 0:100) after addition of fluorescamine. The calculated content of free amino groups of the EXP3174-functionalized polymer was less than 2 % (degree of EXP3174-functionalization > 98 %). The value is marked as a red cross on the calibration line. Results (B-D) represent mean ± SD (n = 3).

Characterization of PEG conformation and validation of nanoparticle morphology

To validate the rigid, tethered and spherically enclosed morphology of both model nanoparticle types, the conformation of the PEG chains in the nanoparticle shell was determined. Therefore, the Flory radius (R_F), which corresponds to the radius of the semispherical volume of a PEG polymer, was calculated and compared to the distance of two grafting sites, *D*, as it has been already described by our group and others[9,10]. R_F is defined by equation 1, where α = 0.35 nm corresponds to the length of a PEG monomer and *[N]* is calculated as the number of monomers in one PEG molecule by dividing the molecular weight of the PEG chain (5000 g mol^{-1}) by the monomer molecular weight of 44 g mol^{-1}.

$$R_F = \alpha \cdot [N]^{\frac{3}{5}}$$

eq. 1

R_F was calculated to be 6.0 nm for the PLA_{10K}-PEG_{5K} block copolymer chains used for the nanoparticle design. The distance, *D*, of two grafting sites in the polymer shell was calculated for both nanoparticle types as shown in equation 2, where *S* corresponds to the surface area that each PEG chain occupies on the nanoparticle surface[11] and is separately defined by equation 3.

$$D = 2 \cdot \sqrt{\frac{S}{\pi}}$$

eq. 2

$$S = \frac{6 \cdot M_{PEG}}{dh \cdot N_A \cdot f \cdot \rho_{NP}}$$

eq. 3

According to equation 3 *S* is defined by the molecular weight of a PEG chain (M_{PEG}), which is related to the (hydrodynamic) diameter of the nanoparticles (*dh*) the mass fraction of PEG in the blends of the PLA_{10K}-PEG_{5K} block copolymer (*f*), and the density of the nanoparticles (ρ_{NP}). A density of 1.25 g cm^{-3} was assumed as a rough estimate for the density of the nanoparticles, a value corresponding to the density of nanoparticles composed of PLA-g-PEG blends.[12] We considered this justified under the assumption that *S* is a circular area, and that the polymer distribution is homogeneous. *D* was calculated for both nanoparticle types (25 %-EXP-NPs and 25 %-EXP-NPs_selenium-containing) to be 1.3 nm. Since R_F was greater than *D*, it could be assumed that the polymer chains adopted a brush conformation. This confirmed the model of rigid, tethered and spherically enclosed nanoparticles.

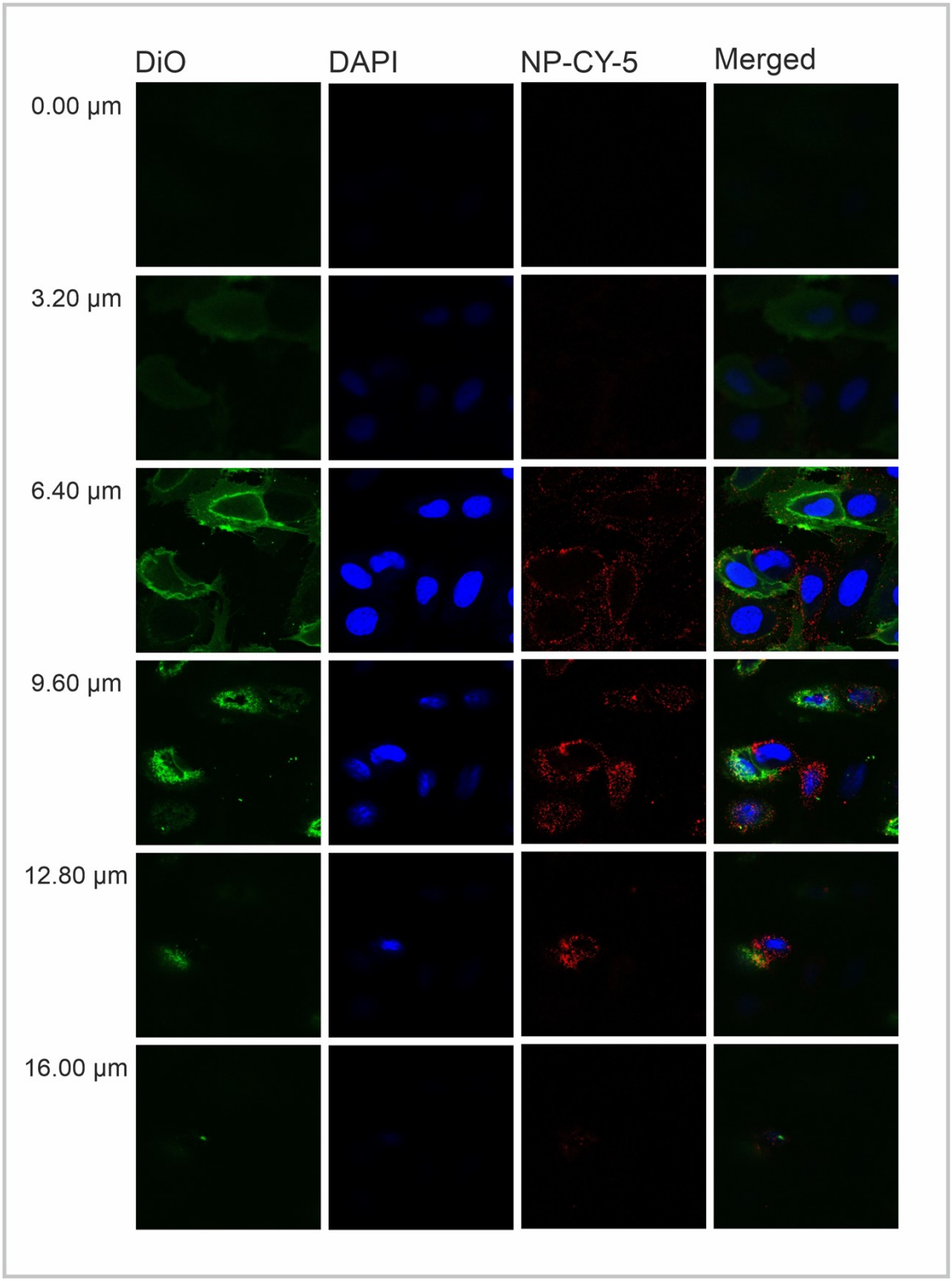

Figure S 6 Confocal laser scanning microscopy Z-stack images of rMCs incubated with a 3 nM fluorescent nanoparticle dispersion at RT to prove particle localization on the cell surface. 25 %-EXP-NPs were obtained by emulsification-solvent evaporation method and fluorescently labelled using CY-5 tagged PLGA. The nanoparticle dispersion was adjusted to 3 nM in Leibovitz's L-15 medium and rMCs were incubated with 200 µL of the dispersion for 30 min at room temperature (22 °C). Cell fixation was performed with paraformaldehyde. Afterwards, cell nuclei were stained with DAPI and cell membranes with DiO. Z-stack images (6 stacks of 3.20 µm) were recorded on a Zeiss LSM 710 (Carl Zeiss Microscopy GmbH, Jena, Germany). Images were processed and analyzed using ZEN 3.5 blue edition software. 25 %-EXP3174 functionalized nanoparticles were mainly localized on the cell membrane, as evident from the merged channel.

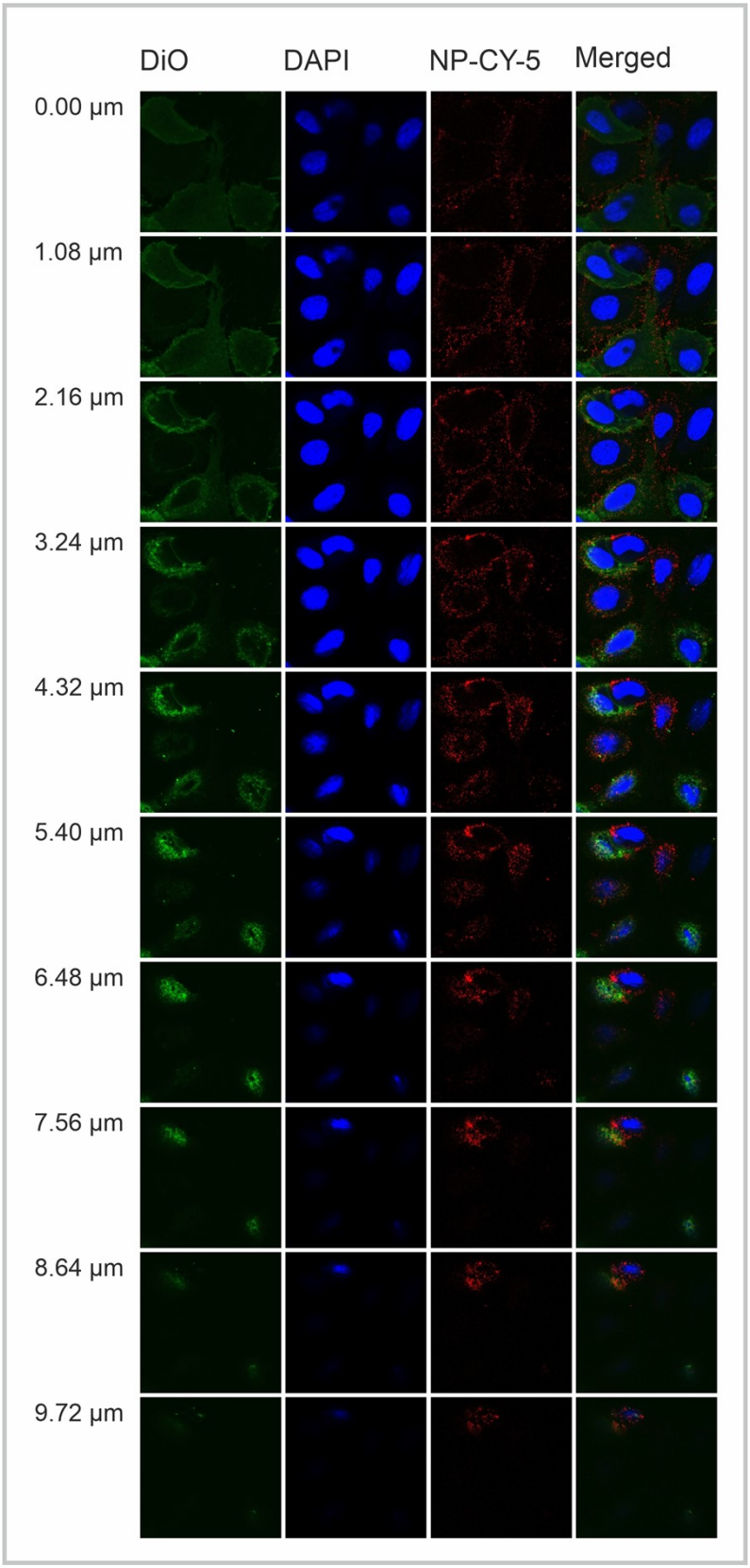

Figure S 7 Confocal laser scanning microscopy Z-stack images of rMCs incubated with a 3 nM fluorescent nanoparticle dispersion at RT to prove particle localization on the cell surface. Further Z-stack images (10 stacks of 1.08 µm) were recorded on the Zeiss LSM 710 (Carl Zeiss Microscopy GmbH, Jena, Germany) for fine resolution. The samples were prepared according to the procedure described above. Images were processed and analyzed using ZEN 3.5 blue edition software. 25 %-EXP3174 functionalized nanoparticles were mainly localized on the cell membrane, as evident from the merged channel.

ICP-OES measurements

ICP-OES measurements were carried out on a Spectroblue ICP-OES (SPECTRO Analytical Instruments GmbH, Kleve, Germany) operating with the software Smart Analyzer Vision. The unit was calibrated against a selenium standard containing 1.000 g L^{-1} selenium (Bernd Kraft GmbH, Duisburg, Germany) in the concentration range from 100 to 16000 ppb. Selenium-containing NPs were produced according to the procedure described in the experimental section. The samples were prepared for measurement by acidic digestion[5,6]. To remove the organic matrix, they were heated in 350 µL of concentrated nitric acid (65 %) (Fisher Scientific, Loughborough, UK) for two hours at 75 °C in a water bath. Subsequently, the tubes were cooled down and samples were diluted in Milli-Q water to a final acidic concentration of 1 M nitric acid. A series of calibrations lines in the concentration range of 0.1 pM to 0.3 nM nanoparticle concentration was recorded to demonstrate successful implementation of selenium in the polymeric matrix and to determine the batch-to-batch deviation in their selenium content. The recorded calibration lines were merged considering the clustering into the data structure.

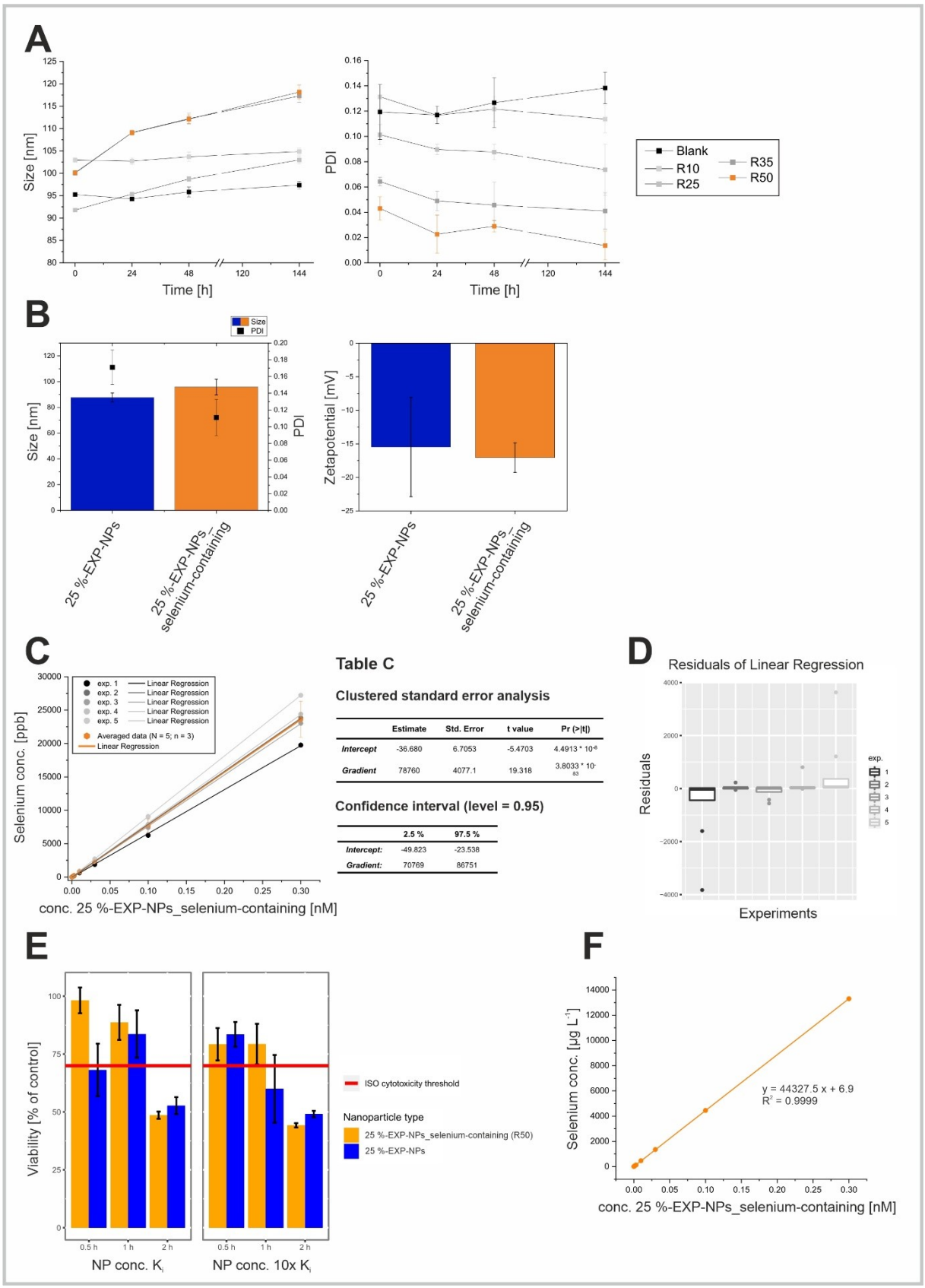

Figure S 8 Implementation of selenium as an ICP-OES/ ICP-MS tag into the polymeric matrix of the model nanoparticles. (A) For the formulation trials of selenium-containing nanoparticles, stability studies on size and PDI, measured by DLS, were conducted on the day of nanoparticle preparation, after 24 hours, after 48 hours and after 144 hours. The data were determined on non-functionalized blank nanoparticles (core: PLGA; shell: PLA_{10K}-PEG_{5K}-COOH), as the ligand is not expected to influence

the amount of stabilizable selenium. Nanoparticles manufactured without the addition of selenium were used as control (Blank). In the formulation trials, the ratio of selenium to PLGA was related as an excess to the ratio of 10.64 mg g^{-1} selenium to polymer published by Luo *et al.*[7] as successfully stabilized. (E.g., R50 described a ratio of 532 mg g^{-1} selenium related to the amount of PLGA used to produce the particles.) All batches of nanoparticles showed increasing size over the course of the study (data shown as mean ± SD, n = 3). As the amount of stabilized selenium increased, the PDI of the batches decreased (data shown as n = 3, mean ± SD). The target formulation, chosen for the further experiments, was marked in orange (R50). (B) Nanoparticle data on hydrodynamic diameters, polydispersity index (PDI) and zeta potential obtained from dynamic light scattering (DLS) measurements. Results represent mean ± SD (N = 5; n = 3). The data sets were tested for normal distribution using the Shapiro-Wilk normality test and for homogeneity of variance using the F-test. Depending on homogeneity of variance the data sets were compared using either Student's two-sample t-test or Welch's two-sample t-test. The two nanoparticle types differed by less than 10 nm in their size (25 %-EXP-NPs: 87.71 ± 3.42 nm; 25 %-EXP-NPS_selenium-containing: 95.82 ± 6.11 nm; Welch´s two-sample t-test, Pr(>t) = $1.872 \cdot 10^{-4}$) and had significantly different PDIs (25 %-EXP-NPs: 0.171 ± 0.021; 25 %-EXP-NPS_selenium-containing: 0.111 ± 0.022; Student´s two-sample t-test, Pr(>t) = $1.813 \cdot 10^{-8}$). We hypothesized that the amorphous selenium served as crystallization nucleus for the polymer matrix and thus contributes to a narrower size distribution, but to a larger particle size in absolute terms. Due to the carboxy-terminated spacer chains, both nanoparticle types showed negative and comparable zeta potentials (25 %-EXP-NPs: -15.48 ± 7.40 mV; 25 %-EXP-NPS_selenium-containing: -17.08 ± 2.12 mV; Welch´s two-sample t-test, Pr(>t) = 0.432). (C) A series of independent calibration lines in the concentration range of 0.1 pM to 0.3 nM nanoparticle concentration of the target formulation (R50) was recorded on a Spectroblue ICP-OES (SPECTRO Analytical Instruments GmbH, Kleve, Germany). Measured values were pooled to a calibration curve (orange). Clustering within the data due to multiple independent measurements was accounted for by processing the data with a clustered standard error analysis. The intercept and gradient, together with the corresponding standard errors, were summarized in ***Table C***. The confidence interval of the calibration line was calculated at the level of 0.95 ***(Table C)***. The negative intercept indicated a limitation of the quantifiability of the selenium content of the nanoparticles by ICP-OES analytics in the lower concentration range. The deviation of the individual batches in their selenium content was calculated at 16.7 %. (D) Plotted residuals of the individual data points to the pooled calculated calibration line. (E) The cytotoxicity of 25 %-EXP-NPs and 25 %-EXP-NPs_selenium-containing (R50) on target cells was determined using MTT-assay.[3,8] In brief, rMCs were seeded at a density of 15,000 cells per well in a 96-well plate and cultured for 24 h (37 °C, 5 % CO_2). Both types of nanoparticles (NP) were manufactured and diluted with Leibovitz's L-15 medium; target cells were incubated for 0.5 h, 1 h and 2 h with NPs adjusted to the concentration of their K_i value and the 10-fold K_i value (10x K_i). RMCs incubated with Leibovitz's L-15 medium served as control. After the incubation period, the samples were discarded and 200 µL of a 1 mg mL^{-1} 3-(4,5-dimethylthiazol-2-yl)-2,5-diphenyltetrazolium bromide (MTT) dilution in RPMI medium were added and incubated for 3 h. Afterwards, the MTT dilution was aspired and 200 µL isopropanol was added. The wells were incubated under gentle shaking and light exclusion for 30 min at RT. The absorbance was then measured at λ = 570 nm and λ = 690 nm on a FLUOstar Omega plate-reader (BMG Labtech, Ortenberg, Germany). Viability was assessed using the difference in absorbance at both wavelengths to the control. Results represent mean ± SD (N = 3; n = 3). In the test-relevant concentrations (K_i / *10x* K_i) and test-relevant time frame (0.5 h), the viability in relation to the control was above the threshold of 70 % specified by the ISO standard (ISO 10993−5:2009 *(Biological evaluation of medical devices, part 5: Tests for in vitro cytotoxicity)*) for both nanoparticle types. (F) A calibration line of 25 %-EXP-NPs_selenium-containing was recorded in the concentration range of 0.1 pM to 0.3 nM nanoparticle concentration using ICP-MS analytics. Dilution steps had to be considered when calculating the selenium content in the cell samples.

		Size (dh/ d) [nm]			Surface (O_{NP}) [nm^2]			Ligand valence (N_L)			Ligands per 100 nm^2
		mean	SD	mode	mean	SD	mode	mean	SD	mode	mean
25 %-EXP-NPs	NTA	81.7	17.5	81.5	21947.9	10071.5	20867.2	4112	3199	3555	19
	DLS	81.1	30.0	78.8	23499.1	18133.0	19517.4	5096	6253	3216	22
	TEM	40.7	13.0	37.1	5747.3	4099.1	4334.4	598	759	337	10
25 %-EXP-NPs_ selenium-containing	NTA	95.1	20.6	82.5	29724.3	20628.2	21382.5	6721	15061	3687	23
	DLS	107.8	39.1	105.7	41320.8	31160.0	35099.4	11804	14093	7755	29
	TEM	47.4	15.0	35.7	7776.0	5351.5	4002.4	932	1133	299	12

Table S 1 Representation of the size (dh/d) [nm], the calculated surface area and the mean ligand valence of the two particle types, 25 %-EXP-NPs and 25 %-EXP-NPs_selenium-containing, as a function of the measurement method used. Data represent as mean ± SD and mode. NTA (NanoSight NS300, Malvern, Worcestershire, UK) and DLS (Malvern Zetasizer Nano ZS, Malvern Instruments, Herrenberg, Germany) raw data were obtained in a triplicate measurement (n = 3). DLS data was analyzed as intensity percent. The size of 500 nanoparticles was measured on six independent sections of each TEM grid.

		NTA concentration measurement	
		Fraction of binding ligands [%]	**Binding ligands/ 100 nm²**
25 %-EXP-NPs	**NTA**	7.5	1.3
	DLS	8.7	1.4
	TEM	65.1	5.3
25 %-EXP-NPs_ selenium-containing	**NTA**	4.7	0.9
	DLS	3.7	0.8
	TEM	41.3	3.9

Table S 2 Maximum fraction of binding ligands and number of binding ligands per 100 nm² nanoparticle surface area (data shown as geometric mean). DLS data was analyzed as intensity percent. For very small nanoparticles in the size distributions, the calculated average binding ligand number exceeded their ligand valence. From a mathematical point of view, this led to values > 1, which were not discriminated against when calculating the geometric mean.

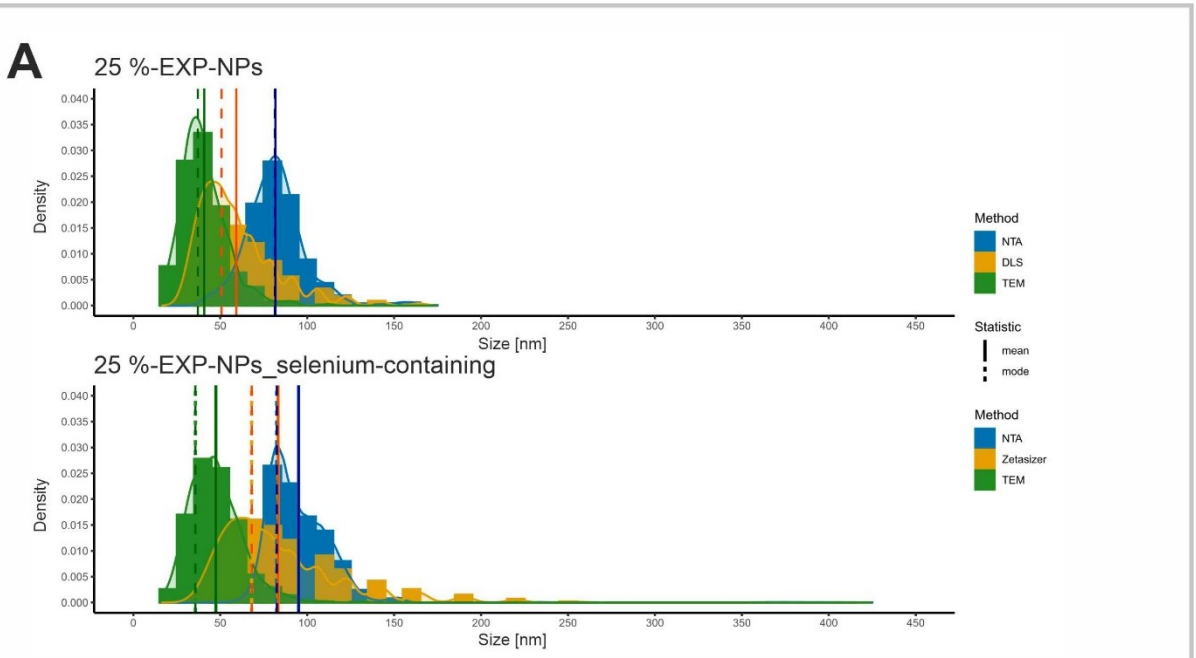

Table A1

		Size (dh/ d) [nm]			Surface (O_{NP}) [nm^2]			Ligand valence (N_L)			Ligands per 100 nm^2
		mean	SD	mode	mean	SD	mode	mean	SD	mode	mean
25 %-EXP-NPs	NTA	81.7	17.5	81.5	21947.9	10071.5	20867.2	4112	3199	3555	19
	DLS	**59.3**	**22.5**	**50.8**	**12611.3**	**11027.2**	**8091.4**	**2064.7**	**3188.2**	**858.3**	**16**
	TEM	40.7	13.0	37.1	5747.3	4099.1	4334.4	598	759	337	10
25 %-EXP-NPs_ selenium-containing	NTA	95.1	20.6	82.5	29724.3	20628.2	21382.5	6721	15061	3687	23
	DLS	**83.2**	**34.5**	**68.1**	**25495.9**	**24468.8**	**14552.4**	**6143.6**	**10402.4**	**2070.3**	**24**
	TEM	47.4	15.0	35.7	7776.0	5351.5	4002.4	932	1133	299	12

Table A2

		NTA concentration measurement	
		Fraction of binding ligands [%]	Binding ligands/ 100 nm^2
25 %-EXP-NPs	NTA	7.5	1.3
	DLS	**22.1**	**2.6**
	TEM	65.1	5.3
25 %-EXP-NPs_ selenium-containing	NTA	4.7	0.9
	DLS	**8.2**	**1.3**
	TEM	41.3	3.9

Figure S 9 Characterization of size and ligand distribution of the model nanoparticles (DLS data shown and analyzed as volume percent). (A) Size distributions of 25 %-EXP-NPs and 25 %-EXP-NPs_selenium-containing plotted as a function of the measurement method. Size values obtained by NTA, DLS, and TEM measurements were compared. Table A1 represents the size (dh/d), the calculated surface area and the mean ligand valence of the two particle types, 25 %-EXP-NPs and 25 %-EXP-NPs_selenium-containing, as a function of the measurement method used. Table A2 represents the maximum fraction of binding ligands and number of binding ligands per 100 nm^2 nanoparticle surface area (data shown as geometric mean).

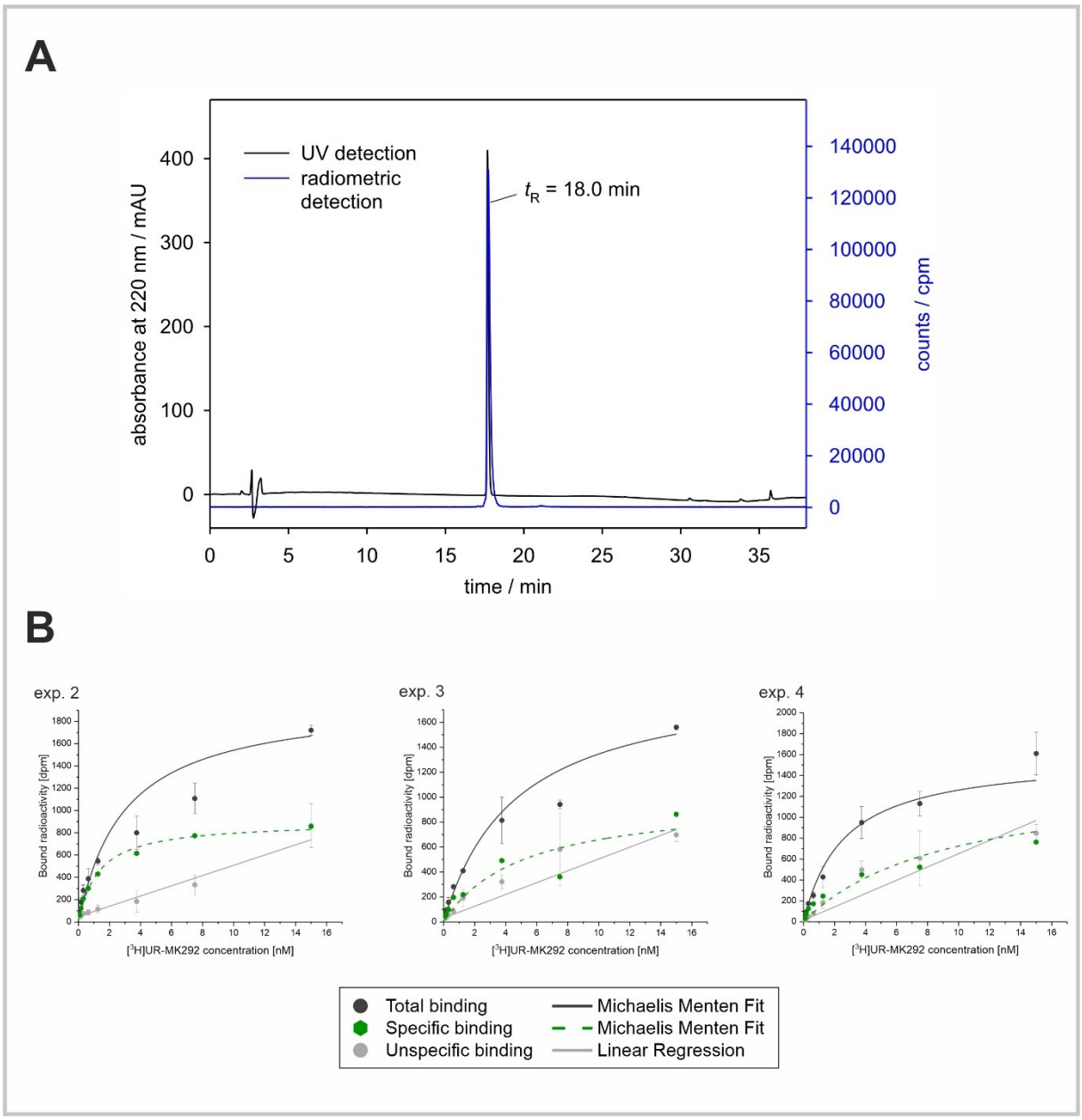

Figure S 10 Determination of the radiochemical purity of [^{3}H]UR-MK292 and radiochemical binding studies with the radioligand on rMCs. (A) RP-HPLC analysis of [^{3}H]UR-MK292 spiked with "cold" UR-MK292, on a system from Waters (Eschborn, Germany) consisting of two pumps 510, a pump control module, a 486 UV/VIS detector, a manual injector, and a Flow-one beta series A-500 radiodetector (Packard, Meriden, USA). Column: Luna C18(2) 150 × 4.6 mm, 3 µm (Phenomenex, Aschaffenburg, Germany). Mobile phase: linear gradient, 0−20 min: acetonitrile + 0.04 % TFA/water + 0.05 % TFA 10:90−38:42, 20−32 min: 38:42−95:5, 32−38 min: 95:5 (isocratic). Flow: 0.8 mL/min. Injection: 100 µL of a solution containing [^{3}H]UR-MK292 (0.2 µM) and UR-MK292 (20 µM). The radiochemical purity of [^{3}H]UR-MK292 was 99 %. (B) Radiochemical saturation binding studies with [^{3}H]UR-MK292 performed to determine the average number of AT1R per cell on rMCs. Data obtained from independent experiments (exp. 2 - 4).

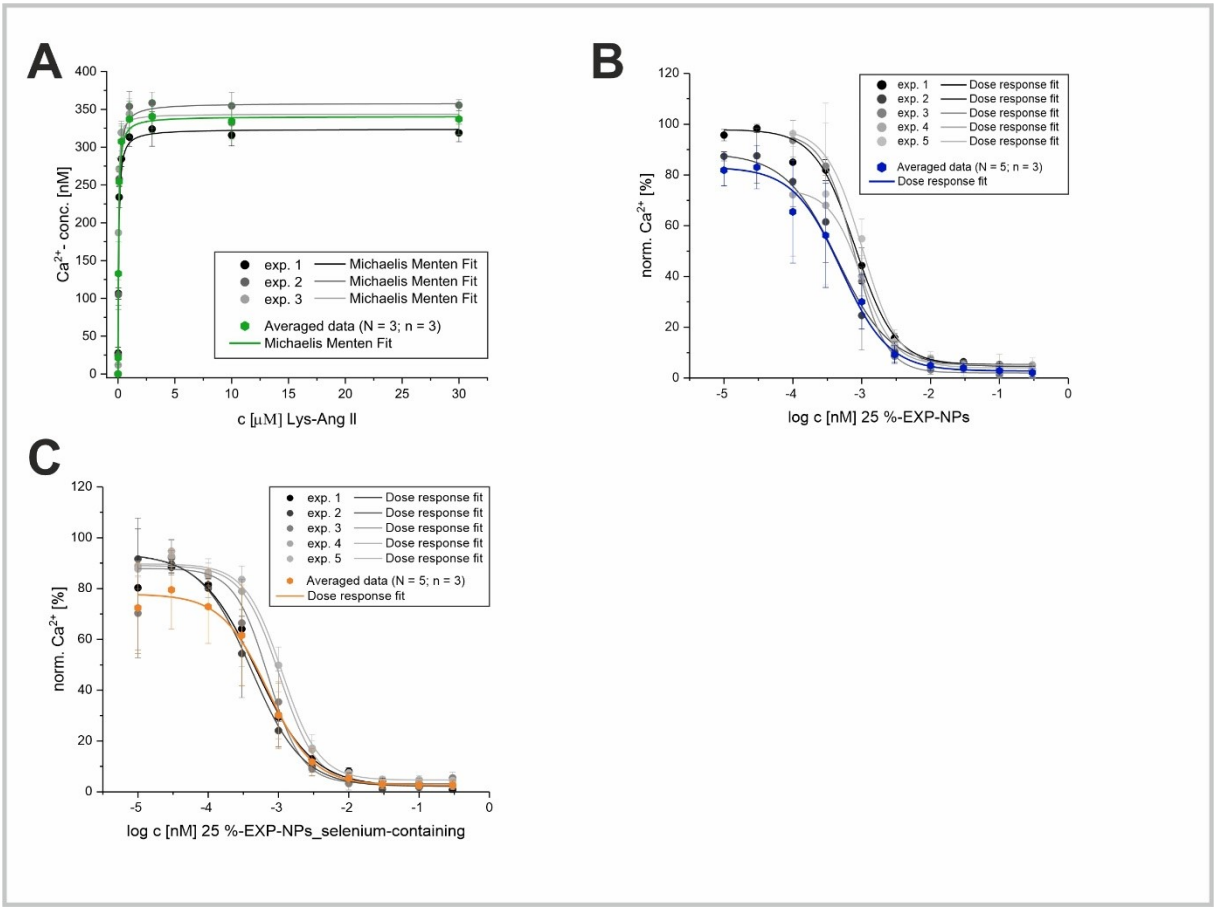

Figure S 11 Saturation and binding curves derived from Fura-2 AM based Ca^{2+} mobilization assay. (A) Saturation curve derived from data acquired for Lys-Ang-II on Fura-2 AM loaded rMCs. Data sets were obtained from three independent experiments (N = 3; n = 3), with the averaged binding curve shown in green and error bars reflecting standard deviation. (B) Serial dilutions of 25 %-EXP-NPs were prepared and measured on Fura-2 AM loaded rMCs. Binding curves were derived from five independent experiments (N = 5; n = 3), with the averaged binding curve shown in blue and error bars reflecting standard deviation. (C) 25 %-EXP-NPs_selenium-containing were manufactured, and binding curves were obtained from five independent experiments (N = 5; n = 3), recorded on Fura-2 AM loaded rMCs. The averaged binding curve is shown in orange, error bars representing standard deviation.

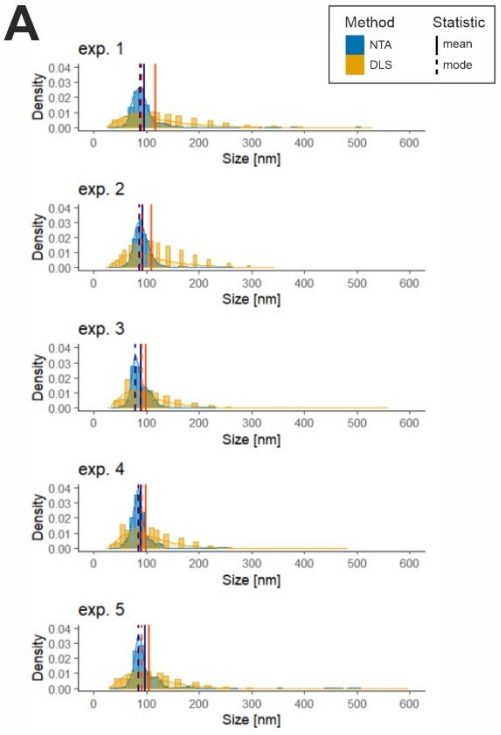

Table A

	25 %-EXP-NPs_selenium-containing					
	NTA dh (nm)			*DLS dh (nm)*		
	Mean	**SD**	**Mode**	**Mean**	**SD**	**Mode**
exp.1	98.7	31.4	94.5	104.7	34.6	91.3
exp. 2/3	85.2	25.8	77.5	120.4	44.8	105.7
exp. 4	91.8	26.8	92.5	108.5	39.1	105.7
exp. 5	93.1	26.4	87.5	108.5	37.0	105.7
Inter-batch SD:	5.5		7.6	6.8		7.2

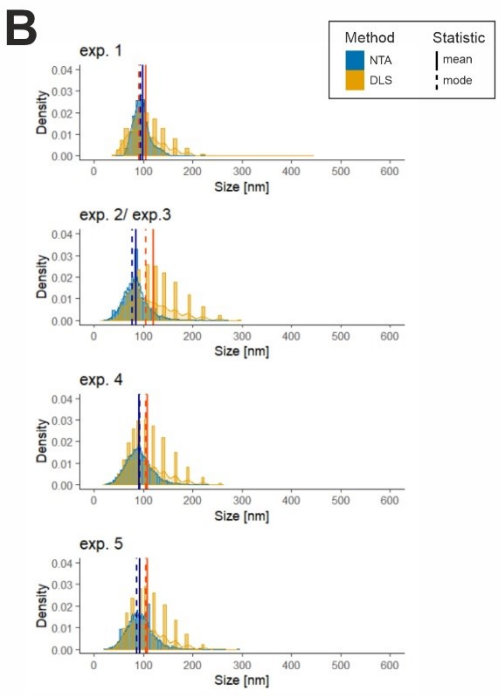

Table B

	25 %-EXP-NPs					
	NTA dh (nm)			*DLS dh (nm)*		
	Mean	**SD**	**Mode**	**Mean**	**SD**	**Mode**
exp.1	96.0	39.8	88.5	117.1	61.9	91.3
exp. 2	92.3	17.9	86.5	110.2	53.5	91.3
exp. 3	89.3	30.3	79.5	99.4	43.0	91.3
exp. 4	89.3	33.9	84.5	99.5	41.8	91.3
exp. 5	98.0	41.0	85.5	105.4	44.2	91.3
Inter-batch SD:	3.9		3.4	7.5		0

Figure S 12 Size distributions of the nanoparticle batches used to determine the K_i values, obtained from NTA (NanoSight NS300, Malvern, Worcestershire, UK) and DLS measurements (Malvern Zetasizer Nano ZS, Malvern Instruments, Herrenberg, Germany). Data were obtained from triplicate measurements (n = 3). (A) 25 %-EXP-NPs and (B) 25 %-EXP-NPs_selenium-containing were manufactured according to the procedure already described. The size distribution of the nanoparticles was measured independently for each batch by NTA and DLS. The obtained data were shown as mean ± SD and mode in the Tables A and B.

Considerations on clathrin coated pit geometry

The geometry of CCPs was simplified to a spherical dome, whose surface area (O_{CCP}) can be calculated using equation 4. Here *r* refers to the radius of the sphere, *a* is the radius of the base circle of the spherical segment and *h* is the height of the spherical dome. The relationship between these variables is shown in equation 5.

$$O_{CCP} = \pi(2rh + a^2)$$ **eq. 4**

$$r^2 = (r - h)^2 + a^2 \leftrightarrow r = \frac{h^2 + a^2}{2h}$$ **eq. 5**

As the CCPs differ in their diameter, *d*, and depth, *h*, depending on their stage of development,[13,14] the parameter ε was introduced to accommodate this (equation 6).

$$\varepsilon = \frac{d}{h} = \frac{2a}{h}$$ **eq. 6**

The geometry of the AT1R was also described by the simplified model of a cylinder with the radius r_R. In a previous study, we calculated the diameter of a single AT1R to be 4.6 nm, and r_R therefore to be 2.3 nm.[10] The membrane area occupied by a single receptor can be determined by equation 7.

$$A_{AT1R} = \pi \cdot r_R^2$$ **eq. 7**

However, this would have assumed that there is no spacing between the individual receptors on the cell membrane. Aldossary *et al.* recently published a study in which they analyzed the distribution and clustering of AT1R on rat pheochromocytoma cells (PC12 cells),[15] which served at least a good approximation to the rat mesangial cells we used due to the origin from the same species. They demonstrated a cluster density of $2.2 \cdot 10^4$ localizations μm^{-2} in AT1R clusters on the cell surface (data represents the mode). Based on their published data, we calculated the minimum area occupied per receptor to be 3.6 nm. The membrane area occupied by a single receptor was therefore described as a function of the radius of the receptor (2.3 nm) and the buffer area, r_B, between the receptors (1.3 nm), as shown in equation 8.

$$A_{AT1R} = \pi \cdot (r_R + r_B)^2$$ **eq. 8**

Based on the assumptions made, the number of AT1R per clathrin coated pit could be estimated by dividing the surface area of the CCP by the membrane area reserved for a single AT1R, as shown in equation 9. For a more accurate estimation, a correction factor for the closest packing of circles (0.907) had to be included in the equation.

$$N_{AT1R/CCP} = \frac{O_{CCP} \cdot 0.907}{A_{AT1R}} = \frac{\left(\pi\left(2rh + a^2\right)\right) \cdot 0.907}{\pi \cdot (r_R + r_B)^2}$$ **eq. 9**

Substituting equations 4-6 into equation 9 yields the following function (equation10) for the number of AT1R depending on ε, *a*, and *h* of the respective CCP.

$$N_{AT1R/CCP}(\varepsilon, a, h) = \frac{\left(\pi\left(\frac{\varepsilon^2 h^2}{4} + h^2 + a^2\right)\right) \cdot 0.907}{\pi \cdot r_R^2}$$ **eq. 10**

References

[1] Abstiens, K. Heteromultivalent Nanoparticles for Selective Targeting of Renal Cells, Universität Regensburg, 2020.

[2] Maslanka Figueroa, S.; Veser, A.; Abstiens, K.; Fleischmann, D.; Beck, S.; Goepferich, A. Influenza A virus mimetic nanoparticles trigger selective cell uptake. *Proceedings of the National Academy of Sciences of the United States of America* **2019**, *116*, 9831–9836. DOI: 10.1073/pnas.1902563116.

[3] Fleischmann, D.; Maslanka Figueroa, S.; Beck, S.; Abstiens, K.; Witzgall, R.; Schweda, F.; Tauber, P.; Goepferich, A. Adenovirus-Mimetic Nanoparticles: Sequential Ligand-Receptor Interplay as a Universal Tool for Enhanced In Vitro/In Vivo Cell Identification. *ACS applied materials & interfaces* **2020**, *12*, 34689–34702. DOI: 10.1021/acsami.0c10057.

[4] Zimmer, O.; Goepferich, A. How clathrin-coated pits control nanoparticle avidity for cells. *Nanoscale horizons* **2023**, *8*, 256–269. DOI: 10.1039/d2nh00543c.

[5] Chaves, E. S.; dos Santos, E. J.; Araujo, R. G.; Oliveira, J. V.; Frescura, V. L. A.; Curtius, A. J. Metals and phosphorus determination in vegetable seeds used in the production of biodiesel by ICP OES and ICP-MS. *Microchemical Journal* **2010**, *96*, 71–76. DOI: 10.1016/j.microc.2010.01.021.

[6] Wheal, M. S.; Fowles, T. O.; Palmer, L. T. A cost-effective acid digestion method using closed polypropylene tubes for inductively coupled plasma optical emission spectrometry (ICP-OES) analysis of plant essential elements. *Anal. Methods* **2011**, *3*, 2854. DOI: 10.1039/c1ay05430a.

[7] Luo, Y.; Ren, Z.; Bo, R.; Liu, X.; Zhang, J.; Yu, R.; Chen, S.; Meng, Z.; Xu, Y.; Ma, Y.*; et al.* Designing selenium polysaccharides-based nanoparticles to improve immune activity of Hericium erinaceus. *International journal of biological macromolecules* **2020**, *143*, 393–400. DOI: 10.1016/j.ijbiomac.2019.12.061.

[8] Abstiens, K.; Fleischmann, D.; Gregoritza, M.; Goepferich, A. M. Gold-Tagged Polymeric Nanoparticles with Spatially Controlled Composition for Enhanced Detectability in Biological Environments. *ACS Appl. Nano Mater.* **2019**, *2*, 917–926. DOI: 10.1021/acsanm.8b02165.

[9] Cruje, C.; Chithrani, D. B. Polyethylene Glycol Functionalized Nanoparticles for Improved Cancer Treatment. *Rev Nanosci Nanotech* **2014**, *3*, 20–30. DOI: 10.1166/rnn.2014.1042.

[10] Maslanka Figueroa, S.; Fleischmann, D.; Beck, S.; Goepferich, A. The Effect of Ligand Mobility on the Cellular Interaction of Multivalent Nanoparticles. *Macromolecular bioscience* **2020**, *20*, e1900427. DOI: 10.1002/mabi.201900427.

[11] Gref, R.; Lück, M.; Quellec, P.; Marchand, M.; Dellacherie, E.; Harnisch, S.; Blunk, T.; Müller, R. 'Stealth' corona-core nanoparticles surface modified by polyethylene glycol (PEG): influences of the corona (PEG chain length and surface density) and of the core composition on phagocytic uptake and plasma protein adsorption. *Colloids and Surfaces B: Biointerfaces* **2000**, *18*, 301–313. DOI: 10.1016/S0927-7765(99)00156-3.

[12] Rabanel, J.-M.; Faivre, J.; Tehrani, S. F.; Lalloz, A.; Hildgen, P.; Banquy, X. Effect of the Polymer Architecture on the Structural and Biophysical Properties of PEG-PLA Nanoparticles. *ACS applied materials & interfaces* **2015**, *7*, 10374–10385. DOI: 10.1021/acsami.5b01423.

[13] Kaksonen, M.; Roux, A. Mechanisms of clathrin-mediated endocytosis. *Nature reviews. Molecular cell biology* **2018**, *19*, 313–326. DOI: 10.1038/nrm.2017.132.

[14] Kozik, P.; Hodson, N. A.; Sahlender, D. A.; Simecek, N.; Soromani, C.; Wu, J.; Collinson, L. M.; Robinson, M. S. A human genome-wide screen for regulators of clathrin-coated vesicle formation reveals an unexpected role for the V-ATPase. *Nature cell biology* **2013**, *15*, 50–60. DOI: 10.1038/ncb2652.

[15] Aldossary, H. S.; Nieves, D. J.; Kavanagh, D. M.; Owen, D.; Ray, C. J.; Kumar, P.; Coney, A. M.; Holmes, A. P. Analyzing Angiotensin II Receptor Type 1 Clustering in PC12 Cells in Response to Hypoxia Using Direct Stochastic Optical Reconstruction Microscopy (dSTORM). *Advances in experimental medicine and biology* **2023**, *1427*, 175–184. DOI: 10.1007/978-3-031-32371-3_19.